Design and optimization of a ducted fan VTOL MAV controlled by Electric Ducted Fans

Yacoubi Moaad[★]*, Jlassi Alaaeddine, Karoun Jawad, Ben Kirane Tarik, Bekkali Lekman, Jhabli Hamza and Hendrick Patrick*[★]
Université Libre de Bruxelles (ULB) - Aero-Thermo-Mechanics department - School of Engineering (Polytechnic School)[★]
Avenue F. D. Roosevelt 50 (CP165/41), 1050 Brussels, Belgium
myacoubi@ulb.ac.be

Abstract

In October 2013, we presented our ducted fan VTOL MAV prototype, Dulbema (see figure 1), in the Journal of Mechanic Engineering and Automation (JMEA).[1] From an aerodynamic study carried out at the Université Libre de Bruxelles (ULB), in pursuit of the latest Minidrones competition issued by the French Aerospace Lab ONERA, the ULB decided to continue the development and optimization of a ducted fan MAV, that was built for this competition and for which VTOL capabilities and autonomous flight were mandatory. This paper explains how we want to increase the maneuverability of our drone.

1. Introduction

Since the first flight of Sikorsky Aircraft Corporation's Cypher UAV in 1992,[2] several concepts of ducted fan have emerged and continue to emerge across the world. The two counter-rotating coaxial rotors, which allowed flight control of the Cypher were giving up due mechanical complexity and replaced by a quadrant of vanes. In the years 2000s, a large number of ducted fan UAVs, equipped with this quadrant of vanes, made their first flights: the iStar (Allied Aerospace - 2000), the Hovereye (Bertin Technologies-2004), the T-Hawk (Honeywell - 2005), the Fantail (Singapore Technology Aerospace - 2006), and many more. They have attempted to join the ducted fan UAV flight control challenge. Nevertheless, most of the projects gave up, sometimes replaced by a conventional helicopter, as for Bertin's Hovereye,[3] definitively skipping the duct advantages in terms of safety, autonomy and relative wind resistance.

Figure 1: The ducted fan MAV of ULB, Dulbema.

It was not until 2014 that a new concept of ducted fan UAV appeared. This one was equipped with several rotors located outside the duct around the main rotor to control the UAV in flight. These models, such as the Hummingbird, promise a flight autonomy of several hours, enough to make investors dreaming and to open new perspectives for the civil UAV market.

In this mad rush towards open market for ducted fan UAVs, we have been working for several years on a prototype equipped with a single rotor, a variable camber stator and a quadrant of vanes, which made its first flight in late 2009. Due to the lack of maneuverability of this prototype, we decided to improve it by replacing the quadrant of vanes

by a quadrotor integrated into the design. To keep the duct benefits, we now use EDF (Electric Ducted Fans) for our new prototype, named SaFly. In this paper, on the one hand, we study the EDF's effects on the performance of our single rotor, and on the other hand, we study the optimal positioning of the four EDF. Various experimental test campaigns have been performed and are presented in this paper, such as smoke flow visualization,[4] to define our new design.

2. Control stages

Dulbema is a ducted fan VTOL (Vertical Take-Off and Landing) MAV (Micro Air Vehicle) with electric propulsion equipped with a two-bladed fixed-pitch rotor that can fly in both helicopter and airplane modes. The rotor is followed by two control stages. The two stages are placed in the rotor induced flow to control the yaw, the roll and the pitch (see figure 2) also at low forward speed.
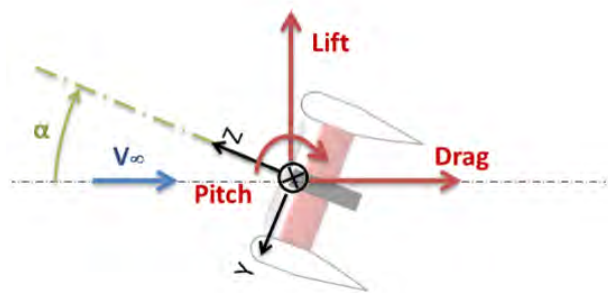
Figure 2: Dulbema lift and drag forces, and pitch moment

A central fuselage contains a part of the avionics components, and the payload can be attached to it. The whole is placed into a duct that has the following aerodynamic profile[5,6] (see figure 3):

- **Toroidal part** that performs better than the classic airfoils leading edge at low angles between the plane of the disc rotor and wind speed. The ideal value of the radius of the torus is : $r_{lip}/D_r = 0.06$.

- **Cylindrical part** to support the first control stage.

- **Divergent part** with a linear slope to maximize the air mass flow by slowing the flow. According to Bernoulli's theorem, the air pressure at the outlet increases. The optimum is to use a ratio of 1.2 between the output and the input surface : $D_{out}/D_r = 1.2$.
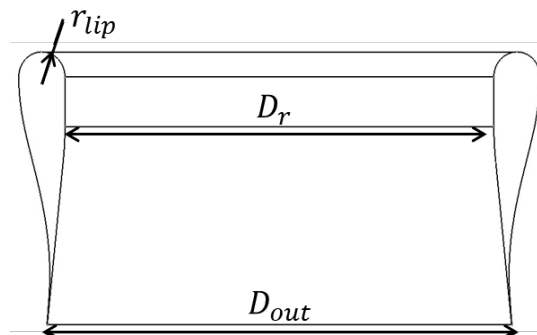
Figure 3: Aerodynamic profile of the duct

During simulations on our ducted fan and during flight tests, we found that there were some areas in the flight envelope where the air speed became zero inside the duct which make the control of the roll and the pitch impossible with our second control stage (for example, during the descent flight due to air recirculation as shown in the figure 4). So we have to find a solution to control the Dulbema in flight.
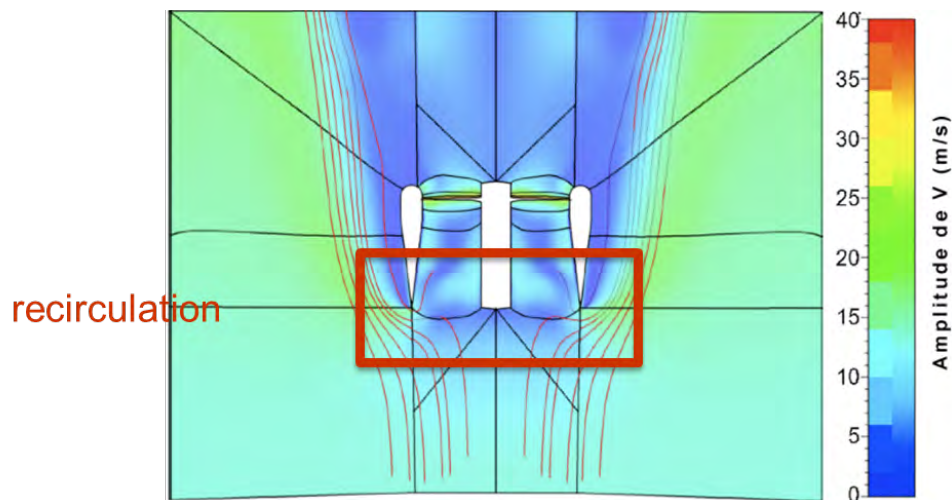
Figure 4: Air flow recirculation

The solution we want to implement is to integrate a multirotor as a control stage for the Dulbema (see figure 5). The state of the art of multirotors, especially quadrotors, can allow us to take a major step forward in order to improve the control of our prototype. In the rest of this paper we will present our research in order to integrate a ducted fan quadrotor into our new prototype, named SaFly.

Figure 5: Safly's control stage for pitch and roll

2.1 Ducted or not ducted

First, it is useful to recall the objectives we set ourselves when we made our prototype. It is important to underline the fact that we want to design a UAV for the civilian market. So we need to:

- land and take off in urban areas,

- provide high payload-to-weight ratio,

- provide high autonomy,

- and give the possibility of operating in an urban environment for civil purposes.

To achieve these objectives we need to design a ducted fan VTOL MAV. So, intuitively, we would like to add a ducted fan quadrotor to keep the advantages of the duct, namely :

- resist wind gusts,

- increase thrust in helicopter mode,

- increase the lift in aircraft mode,

- and protect people and objects in the flight area.

So we will design a ducted fan quadrotor controlled by EDF. This quadrotor will be used to control the roll and pitch. In our case the difference is that the quadrotor is used as the control stage of SaFly (see figure 5). To facilitate the definition of our design, we will first analyze the quadrotor alone. Once we can stabilize it, we will integrate it into the complete prototype.

We plan for a 2:1 thrust to weight ratio, to allow the quadrotor to hover at just half throttle and use the other half for maneuvrability. However, we have to take into account the range of values of the rolling and pitching moments to be countered to stabilize the Dulbema. According to our previous research,[7] we have shown that the moments measured during wind tunnel tests over the entire flight envelope are below 1 Nm for low flight speeds. We therefore decided to choose to have a maximum torque produced by the quadrotor of 1 Nm.

To confirm our intuition to choose a ducted fan, we will verify this theoretically. We will compare the following two configurations : open rotor and ducted rotor. To understand the difference between them we will base on momentum theory. The thrust of a ducted fan is the sum of the variation in the amount of motion induced by the propeller on the fluid and by the duct due to its aerodynamic profile. In general, the latter is 10 to 15% of the rotor thrust defined by the coefficient (k_D). We notice, using the equation 2, that the ideal value of an isolated propeller and a ducted fan propeller are obtained respectively when $k_D = 0$ and $k_D = 1$.

$$P_{OR} = Tv_i = \frac{T^{3/2}}{\sqrt{2\rho A}} \tag{1}$$

$$P_{DR} = T_R v_i = \frac{T^{3/2}}{\sqrt{2(1 + k_D)\rho A}} \tag{2}$$

The power ratio, ducted rotor power (P_{DR}) on open rotor power (P_{OR}) for the same thrust,(see equation 3) allows to estimate the consumption difference between these two configurations. By comparing the ideal case ($k_D = 1$), the ducted rotor consumes 30% less than an open rotor. In the real case ($k_D = 0, 15$) for ducted rotors,the consumption is reduced by 7%.[8]

$$\frac{P_{DR}}{P_{OR}} = \frac{1}{\sqrt{1 + k_D}} \tag{3}$$

The figure 6 represents the power required to produce 200 g_F[1] of thrust. We notice that the difference in power consumption decreases as the diameter increases. As a result, we can see that the utility of a ducted fan disappears for large diameters.

3. Fan modelisation

The sizing of our propulsion chain with EDF will not be presented here. However, it is important to note that since few aircraft models use this type of propulsion chain, we have limited informations about them and we have to do our own experiment.The non existence of the CW (Clock Wise) EDF in the market leads us to design the fan by ourselves. To do this, there are several ways: generate the 3D model of the manufacturer's fan with a 3D scanner, mathematical modeling, cut a fan at different radius to recover the different profiles,... We have decided to model our fan mathematically and this in order to be able to produce our own fans.

---

[1]Gram-force
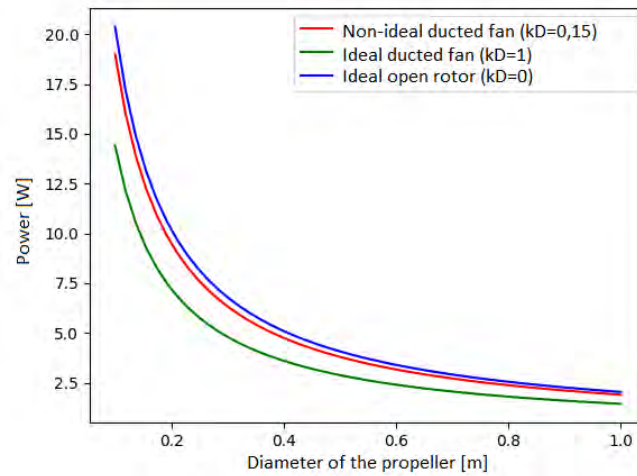
Figure 6: Power as a function of rotor diameter (isolated and ducted) to produce a 200 g_F thrust

3.1 Blade Element Theory

The design of the propeller is determined on the one hand by reverse engineering by retrieving some key geometric dimensions from the existing model and on the other hand by using blade element theory. The Blade Element Theory (BET) was first proposed by Stefan Drzewiecki in 1892 to analyze aircraft propellers. The momentum theory (Froude's theory) is a simple and effective method to provide an order of magnitude of the power required. The latter is mainly based on fluid dynamics by highlighting the variation in the amount of movement. This approach is not adequate to design the propeller in question. Indeed, momentum theory does not take into account the following parameters :

- Number of blades

- Characteristics of the profiles along the blade (e. g. lift and drag coefficients)

- The blade twist

- The compressibility effect

- ...

On the other hand, BET takes into account all these important parameters for the generation of the 3D model. The method consists in considering that each blade is a succession of profiles producing a resultant of aerodynamic force in the plane of it, see figure 7. The total result is obtained by integrating the aerodynamic forces in two dimensions along the radius.

On the figure 7 is represented the lift force $\overrightarrow{dL}$ perpendicular to the relative speed $\overrightarrow{U}$ and the drag force $\overrightarrow{dD}$ parallel to the relative speed. The resultant of these aerodynamic forces is represented by the force vector $\overrightarrow{dR}$. The thrust force $\overrightarrow{dF_z}$ is obtained simply by projecting the vector $\overrightarrow{dR}$ in the direction of movement, here the axis $\overrightarrow{e_z}$, and the force $\overrightarrow{dF_x}$ generating the anti-torque is the projection along the axis $\overrightarrow{e_x}$. The speed triangle is defined by the rotation speed $\overrightarrow{U_T}$ and the axial speed $\overrightarrow{U_P}$. The relative velocity $\overrightarrow{U}$ is deduced from the two previous velocities by the Pythagorean theorem by the relationship 4. The angle of the profile θ is the algebraic sum of the angle of attack α and the angle of the velocity triangle ϕ.

$$\overrightarrow{U} = \overrightarrow{U_T} + \overrightarrow{U_P} \tag{4}$$

$$U_T = y\Omega \tag{5}$$

5

DUCTED FAN VTOL MAV
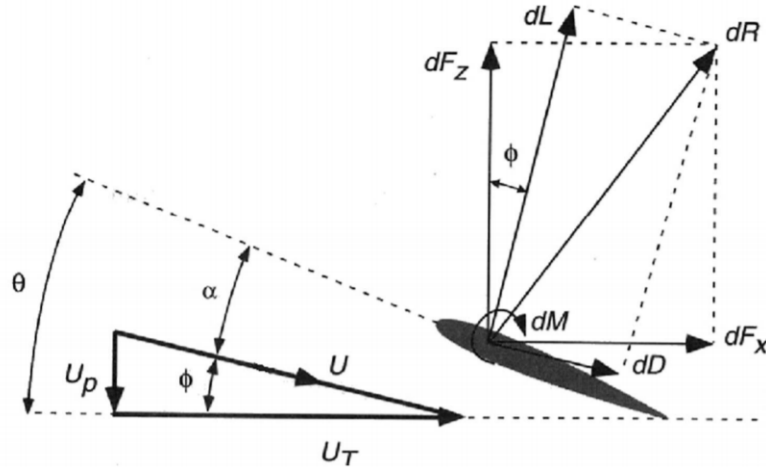
Figure 7: Model representing the different forces acting on the profile and the corresponding triangle velocity
(source : Blade Element Theory (BET), Helicopters, by Filipe Szolnoky Cunha, slide 5)

With y the radius in meters and *Omega* the rotation speed in radians per second. r_0 is the radius at the root (*Root*), R is the tip radius (r_{tip}) and dy is an infinitesimal radius difference. We can now calculate the lift $\overrightarrow{dL}$, drag $\overrightarrow{dD}$, thrust $\overrightarrow{dF_Z}$ and anti-torque $\overrightarrow{dF_X}$.

$$dL = \frac{1}{2}\rho U(y)^2 c(y) C_L dy \tag{6}$$

$$dD = \frac{1}{2}\rho U(y)^2 c(y) C_D dy \tag{7}$$

$$dF_Z = dT = N_B(dL\cos\phi - dD\sin\phi) \tag{8}$$

$$dF_X = dQ = N_B(dLy\cos\phi + dDy\sin\phi) \tag{9}$$

With $c(y)$ the rope in meters varying along the radius. As a measure of the existing model, the chord at the root c_{root} is 0.016 m and at the tip c_{tip} is 0.011 m. Where r_0 (r_{root}) and R (r_{tip}) are 0.015 and 0.031 m respectively. Therefore, $c(y)$ can be calculated by the equation 10. From the vector equation 4, we can calculate $U(y)^2$ (see equation 11). The number of blades is represented by the variable N_B (positive integer with a minimum of 2). The angle ϕ is deduced by the relationship 12.

$$c(y) = -0,3125y + 0,0207 \tag{10}$$

$$U(y)^2 = (\Omega y)^2 + U_P^2 \tag{11}$$

$$\phi(y) = \arctan\left(\frac{U_P}{\Omega y}\right) \tag{12}$$

The total thrust T as well as the torque Q generated by the propeller are obtained by integration along the radius r_0 to R :

$$T = \frac{1}{2}\rho N_B \int_{r_0}^{R} U(y)^2 c(y) \left[C_L(\alpha)\cos(\phi(y)) - C_D(\alpha)\sin(\phi(y))\right] dy \tag{13}$$

$$T = \frac{1}{2}\rho N_B \int_{r_0}^{R} ((\Omega y)^2 + U_P^2)(-0,3125y + 0,0207)\left[C_L(\alpha)\cos\left(\arctan\left(\frac{U_P}{\Omega y}\right)\right) - C_D(\alpha)\sin\left(\arctan\left(\frac{U_P}{\Omega y}\right)\right)\right] dy \tag{14}$$

$$Q = \frac{1}{2}\rho N_B \int_{r_0}^{R} U(y)^2 c(y) y \left[C_L\sin(\phi(y)) + C_D\cos(\phi(y))\right] dy \tag{15}$$

$$Q = \frac{1}{2}\rho N_B \int_{r_0}^{R} ((\Omega y)^2 + U_P^2)(-0,3125y + 0,0207)y\left[C_L(\alpha)\sin\left(\arctan\left(\frac{U_P}{\Omega y}\right)\right) + C_D(\alpha)\cos\left(\arctan\left(\frac{U_P}{\Omega y}\right)\right)\right] dy \tag{16}$$

3.1.1 Design point

The starting point depends on the definition of our objectives. We decided to choose thrust as the design point. This one takes the value of 500 g_F. We have mesured the rotational speed for this thrust : 33.424 RPM [2]. We can now estimate the axial velocity from the momentum theory (see equation 17). The outer and inner diameters of the propeller supplied by the manufacturer are respectively 61,5 and 29,76 mm.

$$U_P = \sqrt{\frac{T}{\rho A}} = \sqrt{\frac{0,5.9,81}{1,225.0,0023}} = 41,7 \text{ m/s} \tag{17}$$

The angle ϕ can be calculated by the simple knowing U_T, Ω, r_0 and R. The variation of the angle ϕ is normally not linear by the presence of arctangent but let us consider it, for simplicity, according to a linear trend $y = -1090x + 56.81$. The blade angles θ at the root and tip blade can be easily deduced as follows :

$$\theta_{root} = \alpha + \arctan\left(\frac{U_P}{\Omega r_0}\right) \tag{18}$$

$$\theta_{tip} = \alpha + \arctan\left(\frac{U_P}{\Omega R}\right) \tag{19}$$

The deduction of the angle of attack α can only be made when we know the profile.

3.1.2 Profile choice

Several literature, including[9] and,[10] propose the use of the profile **NACA4412**. This profile has very good performance at low and high speeds. The aerodynamic coefficients depend on the Reynolds number Re.

$$Re = \frac{U.c}{\nu} \tag{20}$$

Through the equation 20, we can calculate the Reynolds number at the root Re_{root} and at the end of the blade Re_{tip}. They are respectively, for a kinematic viscosity of $1,51x10^{-5}$ to $20°C$, 44..185 and 30377. The closest value to Re, offered by the Airfoil Tools website, is 50.000. Therefore, the graphs giving the coefficients of lift, drag and ratio of the latter two are represented respectively by the following figures 8. We note three important key points :

- the lift stalls at about 9°**??**,

- the minimum drag is about 0°,

- and the maximum C_l/C_d ratio is 8,5°.

The maximum propeller performance is obtained when the maximum C_l/C_d ratio is reached. Indeed, at this point, we have the highest lift for a minimum of drag. As a result, the engine will provide less power, since the resistive torque depends on drag, for a predefined thrust. However, the drag for this angle of attack ($\alpha = 8,5°$) is at the ends of the minimum drag. Therefore, a small variation in the angle of attack can lead to an exponential increase in the drag coefficient C_d. The compromise is to find the minimum drag while having a significant coefficient of lift. We chose, for simplicity and in the first instance, an angle of attack of 2°. This value was influenced by the attack angles used in [9] and [11].

We can now calculate the angles at the root θ_{root} and the tip of the blade θ_{tip}. With the knowledge of these angles, the profile used and some geometrical dimensions of the propeller provided by the manufacturer, it is now possible to generate the 3D file (see figure 9). It should be noted that the leading edges are not tapered on the figure 9. Indeed, SLS polyamide printing [3] cannot tolerate thicknesses less than 0,8 mm. We will analyse during the tests if this reduces the performance of the blades.

---

[2]Rotation Per Minute
[3]Laser powder sintering
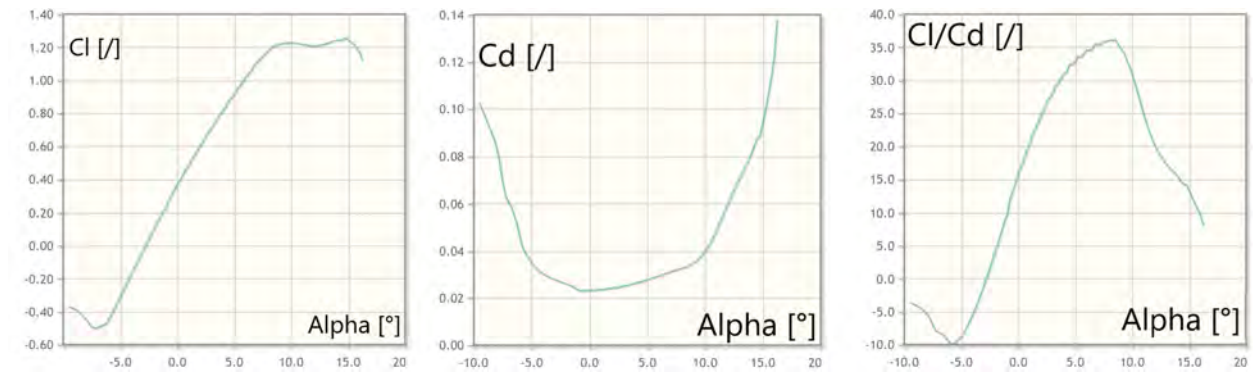
Figure 8: Coefficient of lift, drag and their ratio as a function of the angle of attack[12]

$$\theta_{root} = 2 + \arctan\left(\frac{41,7}{3500.0,015}\right) = 40,46° \tag{21}$$

$$\theta_{tip} = 2 + \arctan\left(\frac{41,7}{3500.0,031}\right) = 23,02° \tag{22}$$
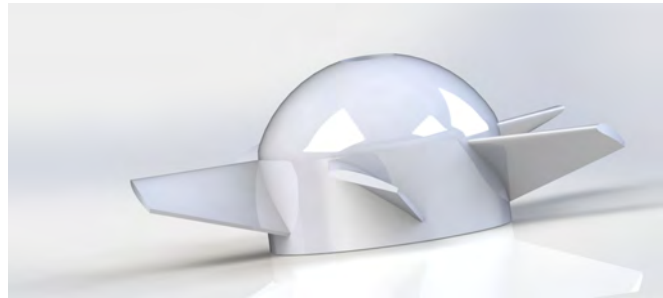
Figure 9: 3D modeling of a CW propeller on SolidWorks

4. Make the invisible visible

In this section, we will explain how to visualize the air flow behaviour. There are different methods to visualize it quantitatively or qualitatively.[4] We will perform a qualitative analysis in order to obtain a first idea of the air flow behaviour quickly and at a lower cost to define our new design. The purpose here is to analyze the impact of the main rotor on an EDF. Then, to analyze the impact of the EDF on the main rotor. In a second phase, we will analyze the air flow using a PIV system (Particle Image Velocimetry) in a wind tunnel. This will not be the subject of this paper.

4.1 Smoke flow visualisation

The first method we choose is the smoke flow visualisation. This method is simple to implement and does not require significant financial and technical resources. A good camera with enscens and an image processing software are enough to obtain usable qualitative results.

The shooting must be done under maximum dark conditions. Indeed, too much brightness obscures the smoke and does not highlight the air flow behaviour.

A dark room has been made with flash as the only light source. The camera is fixed on a tripod to prevent any movement when shooting that could blur the image. Since no light enters the darkroom, we need to adjust the photo settings to see something through the lens of the camera.

The first parameter to adapt is the shutter speed. A shutter speed that is too long will result in a picture too much bright, while a smaller shutter speed will offer little light. Added to this is a blur effect that occurs when the shutter speed is smaller than 1/60 of a second, even if the camera is on a tripod, that can produce shaking movement when the user clicks on the shutter button for example. The 1/60 second limit is the chosen value.

The second parameter is the opening of the diaphragm, which was fixed at F.7, an opening small enough to not let in too much light to the point of overexposing the photo (an overexposed photo is a completely white photo). In addition, this opening value offers the advantage of providing a limited depth of field and thus isolating the EDF and smoke.

The last parameter to adapt is the sensitivity of the sensor cells of the camera, called ISO. The smallest possible value is the one chosen, namely 100 ISO, because pushing the ISO too high would cause a loss of quality of the shoot.

Before observing the behaviour of the air flow, we will define a test area. After analysing the state of the art, we decided to take as analysis points (see figure 10) the Hummingbird ducted fans position (point A), the Fantail vanes position (point D), and a reference point (point R). After observing a decrease of more than 25% for position D, we completely abandoned this possibility. Position A reduces the thrust by 5% compared to our reference point. So we tried to improve this by moving the duct upwards to keep it away from the effect of the main rotor (position B and C). This time the thrust is better and, for position C, we have a thrust 2% higher than our reference point. We tested around this area (C',Cd,Cdd,Cg) and the point C remains the highest value. We then defined a zone (green triangle on the figure) in which our EDF must be placed to obtain better performances. Placing the EDF in C requires a heavier structure to fix the EDF on the prototype than to get closer to R. Therefore, we decided to take the point P in order to have a lever arm big enough to generate our maximum torque of 1 Nm to counter the rolling and pitching moments.

Point	(X;Y;Z) position	EDF's thrust [N]
R	(0;0;10)	5,21
A	(40;0;-20)	4,91
B	(40;0;10)	5,06
C	(40;0;30)	5,31
D	(10;0;-50)	3,81
C'	(40;0;30)	5,31
Cd	(40;0;35)	5,31
Cg	(40;0;25)	5,16
Cdd	(40;0;40)	5,16

Table 1: EDF's thrust for each positions

After that, we will visualize the air behavior for positions R, C and P (see figure 10). The figure 11 shows the results obtained for EDF on the one hand and the Dulbema UAV on the other hand. We can already see that the Dulbema, equipped with a two-bladed rotor followed by four blades stator, has a turbulent flow. In comparison, EDF's air flow is laminar. This turbulence is due to propeller vibrations. Indeed, every quarter turn the two-bladed rotor induced flow pushes on the stator blades and this generates shocks. We will therefore replace our rotor with a three-bladed one to reduce these vibrations.

Figures 12, 13 and 14 represent the air flow for respectively the R,C and P positions. We can see that the C position strongly disrupts the air flow entry at the duct edge. As a result, we lose the lift generated by the duct inlet, reducing the increase of the rotor thrust produced by the duct, which is not to our advantage. For this reason, we will focus on position P.

4.2 Laser tomoscopy

The second method is laser tomoscopy. The specificity of this method is that it allows the flow to be visualized on a 2D slice quickly and at a lower cost, compared to a conventional wind tunnel equipped with a PIV (Particle Image Velocimetry) system that shows the flow in 3D with quantitative results.To obtain the final results, after filming the air flow, image processing will be used. Like the precedent methode, the process requires a dark room, a very high
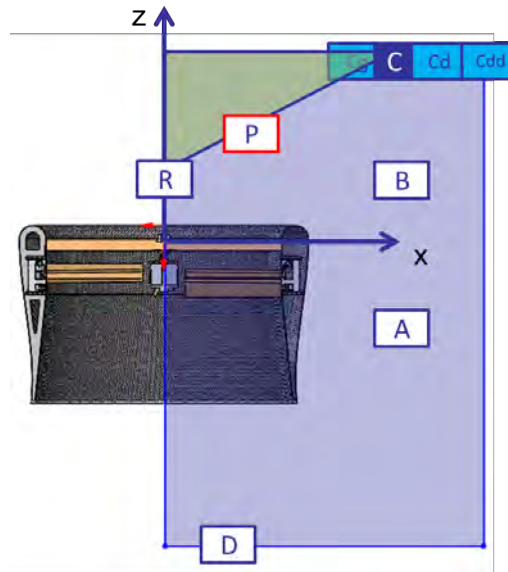
Figure 10: EDF's positions

Figure 11: Smoke visualisation results obtained for Dulbema (left) and EDF (right)

Figure 12: Smoke visualisation test for the reference position

definition camera with a large FPS and smoke (produced by incense in our case). We just need to add a laser light in place of the flash light and to replace the isolated pictures by video.

Taking video is similar to taking pictures except that it is of course not possible to set the shutter speed of a video. As a result, the video may appear less stable. The chosen values of ISO and aperture are exactly the same for videos as for photos.

Our two laser tomoscopy test benches are shown in figure 15. In the dark we can see the smoke only in the laser slice that makes the invisible visible.

Figure 13: Smoke visualisation test for the C position

Figure 14: Smoke visualisation test for the P position
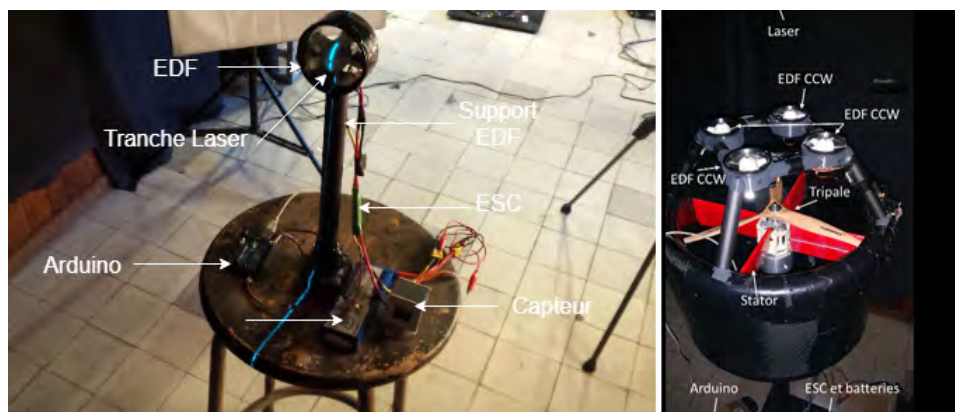
Figure 15: Smoke and laser test bench for EDF (left) and SaFly (right)

We can see in the figure 16 that the air flow behaves in a similar way and corresponds to the usual air flow of a ducted fan. In fact, at the inlet of the EDF, the flow converges well towards the rotor and have a laminar behavior compared to the turbulent flows that appear in figure 11. It is also observed that the air is returned from downstream to upstream at the tip of the duct that forming a thrust on the tip of the duct that increases the total thust produced by the EDF. At the exit of the duct, we observe a straight current tube, imposed by the duct, which prevents its natural contraction.

It can also be seen that the inlet air tube for the printed CW propeller is contracted. This is due to the fact that

for the CW propeller, the results are less efficient than the CCW. We think this is probably due to the printing and we need to investigate this. Since the CW propeller must rotate faster to provide 200 g_F of thrust, it is therefore normal for the upstream air flow to be more contract.

Figure 16: Visualization of the flow for 200 g_F from left to right: CCW manufacturer, CW printed, CCW printed

5. Static test bench

We will use in this section another test bench to measure the thrust of our different propellers (see figure 17. The figure 18 shows us the results obtained in terms of current consumption in function of the thrust for the manufacturer's propeller and the printed propellers. We notice that there is a great similarity between these two propellers. When the thrust is very low (< 100 g), the consumption is lower for the printed propeller. Above 300 g_F of thrust, the propeller proposed by the manufacturer dominates. This difference is mainly due to the difference in weight of the two propellers.

Figure 17: Thrust test bench

Indeed, the printed propeller has been reinforced for safety reasons. In addition, the trailing edge has been removed (restrictions on the 3D printing machine, the minimum thickness is limited to 0.8 mm). Other parameters can also affect the propeller efficiency : vibrations because the propeller has not been balanced, the twisting of the blades, roughness,.... The list is not exhaustive.

6. Conclusion

All of this allowed us to validate the design of our 3D printed propellers. On the one hand, it can be seen that the gap between the manufacturer propeller and the printed propeller is acceptable. On the other hand, we observe that the air flow is not negatively affected by the printed propeller. Therefore, we will be able to use our CCW and CW printed propellers for our tests on our prototype. This will save us from having to use complex and expensive manufacturing methods (moulds, injection,...).
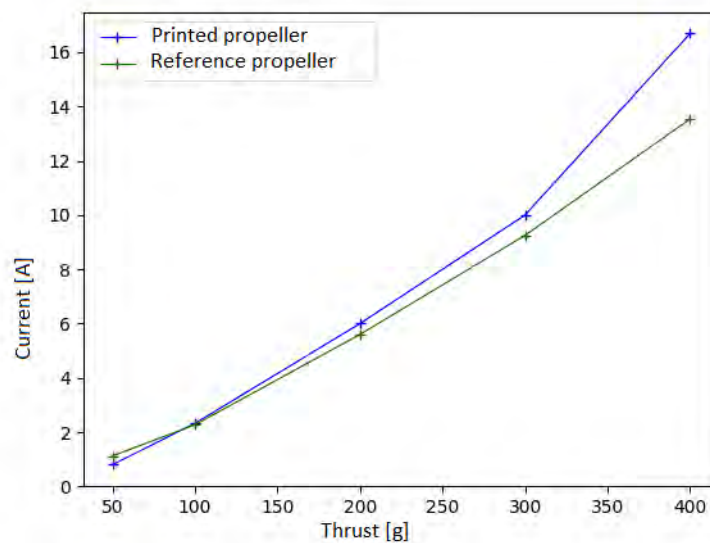
Figure 18: Comparison between the power consumption of the manufacturer's fan (in green) and the printed one (in blue)

7. Acknowledgments

References

[1] Moaad YACOUBI1 and Patrick HENDRICK. A ducted fan mav anti-torque control system. *Journal of Mechanics Engineering and Automation*, 3(10):609–617, Jun-October 2013.

[2] A. Angrand. Sikorsky cypher, air & cosmos. 1818(16):20, Nov. 2001.

[3] Paolo Binetti, Daniel Trouchet, T Hamel, Lorenzo Pollini, Mario Innocenti, and Florent Le Bras. The flight control system of the hovereye vtol uav. 05 2007.

[4] Slavica Ristić. Flow visualisation techniques in wind tunnels. *Military Technical Institute (VTI), Ratka Resanovića 1, 11132 Belgrade, SERBIA*, Vol. LVII(No. 1), 2007.

[5] Herman S Fletcher. Experimental investigation of lift, drag, and pitching moment of five annular airfoils. *National Advisory Committee for Aeronautics. Langley Aeronautical Lab.; Langley Field, VA, United States*, NACA Technical Note 4117(NACA-TN-4117):28 pages, Oct. 1957.

[6] Robert T Taylor. Experimental investigation of the effects of some shroud design variables on the static thrust characteristics of a small-scale shrouded propeller submerged in a wing. *National Advisory Committee for Aeronautics. Langley Aeronautical Lab.; Langley Field, VA, United States*, NACA Technical Note 4126(NACA-TN-4126):26 pages, Jan. 1958.

[7] A. Alami E. Kagambage G. Dimitriadis P. Hendrick F. Buysschaert, M. Yacoubi. Development and evaluation of a vtol observation platform. *27th Congress of International Council of the Aeronautical Sciences*, (Paper ICAS2010-1.6ST1), Nov. 2010.

[8] James E. Benini James C. Wallace II Dr. Michael McInerney Rose-Hulman Brian Hirsch Mike Dason Marcus Songer Kamal Yadav Chris Fitzgerald Dr. Patrick Ferro, Tristan Linck. Hovercraft thrust duct, 2004.

[9] Jan Kubica. Electric ducted fan theory, August 2017.

DUCTED FAN VTOL MAV

[10] Stuart Sherlock. Compressibility: Selection of propeller airfoil section. (prandtl-glauert rule).

[11] Eric Savaterro et Claude Goumai André Paris. Mécanique du vol - cours théorique ppl, 2016.

[12] Profil naca4412. http://airfoiltools.com/airfoil/details?airfoil=naca4412-il. [Consulté le 30 mai 2019].